Three-phase nanocomposites of two nanoclays and TiO$_2$: Synthesis, characterization and photocatalytic activities

Dimitrios Papoulis [a,*], Sridhar Komarneni [b], Dionisios Panagiotaras [c], Elias Stathatos [d], Konstantinos C. Christoforidis [e,f], Marcos Fernández-García [e], Huihui Li [g], Yin Shu [g], Tsugio Sato [g], Hiroaki Katsuki [h]

[a] Department of Geology, University of Patras, 26504 Patras, Greece
[b] Materials Research Institute, 205 Materials Research Laboratory, The Pennsylvania State University, University Park, PA 16802, USA
[c] Laboratory of Chemistry, Department of Mechanical Engineering, Technological Educational Institute (TEI) of Western Greece, 26334 Patras, Greece
[d] Department of Electrical Engineering, Technological Educational Institute (TEI) of Western Greece, 26334 Patras, Greece
[e] Instituto de Catálisis y Petroleoquímica, CSIC, C/Marie Curie 2, 28049 Madrid, Spain
[f] Department of Materials Science and Engineering and Chemical Engineering Universidad Carlos III de Madrid, Avenida de la Universidad 30, 28911 Leganés, Spain
[g] Institute of Multidisciplinary Research for Advanced Materials, Tohoku University, Sendai 980-8577, Japan
[h] Saga Ceramics Research Laboratory, 3037-7, Arita-machi, Saga 844-0022, Japan

ARTICLE INFO

ABSTRACT

For the first time two different nanoclay minerals were combined with nanophase anatase for the synthesis of three-phase nanocomposites with improved photocatalytic properties. The novel halloysite (H) + palygorskite (Pal)–TiO$_2$ nanocomposites were prepared using palygorskite and halloysite from Greece. Three nanocomposites were synthesized using [Hal + Pal] to TiO$_2$ mass ratios of [10 + 20]:70, [15 + 15]:70 and [20 + 10]:70, respectively by depositing anatase form of TiO$_2$ on the clay surfaces using titanium isopropoxide as a precursor under hydrothermal treatment at 180 °C. Phase composition, particle morphology and physical properties of these three-phase nanocomposites were characterized by XRD, ATR–FTIR, SEM, TEM, DR-UV–Vis, N$_2$-adsorption/desorption isotherms. The photocatalytic activities of three-phase clay–titania nanocomposites in decomposing NO$_x$ gas and toluene vapor were determined. The three-phase clay–titania nanocomposites showed significantly higher photocatalytic activity in decomposing inorganic and organic pollutants compared to that of either palygorskite- or halloysite–TiO$_2$ nanocomposites under both UV- and visible-light irradiation. These studies led to a new class of clay-based nanocomposite materials with advanced photocatalytic properties.

1. Introduction

Ultra fine TiO$_2$ powders, especially in the form of anatase, have good catalytic activities because of their large specific surface areas as surfaces are where reactions take place [1]. Anatase has also been proven to be among the most suitable semiconductors for widespread environmental applications such as the decomposition of many air and organic pollutants [2–4]. An important drawback of anatase powders is that they easily agglomerate into larger particles, resulting in an adverse effect on catalyst performance [1]. Many clay minerals have been used to synthesize nanocomposites with TiO$_2$ (especially anatase) to reduce anatase agglomeration

problem and to enhance the decomposition of organic and inorganic pollutants by photocatalytic degradation [4–6]. Intercalation of TiO$_2$ nanoparticles in the clay mineral structure allowed to obtain the high initial dispersion, prevented their aggregation and enhanced their photocatalytic activities [6–8]. Previous experiments (single clay nanocomposites) also showed that using clay minerals with microfibrous morphology increased TiO$_2$ photocatalytic activity [9,10]. Recent studies revealed that dispersing the TiO$_2$ particles onto fibrous palygorskite [4,11] or tubular halloysite [12] surfaces under mild conditions is a promising method to obtain and maintain highly dispersed TiO$_2$ under reaction conditions.

In this paper we describe the novel synthesis and characterization of nanophase TiO$_2$ particles supported on a mixture of two different clay minerals with different morphologies, palygorskite (fibrous morphology) and halloysite (tubular morphology) in three different proportions, using a simplified method under mild

* Corresponding author. Tel.: +30 2610 997842; fax: +30 2610 997560.
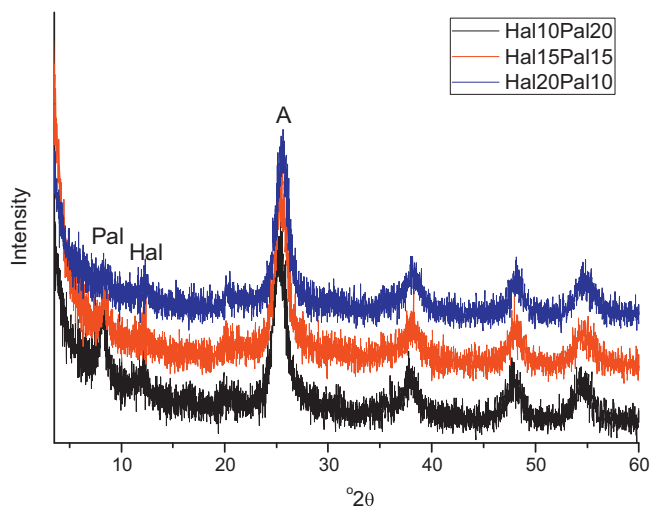E-mail address: papoulis@upatras.gr (D. Papoulis).

Fig. 1. XRD patterns of three phase nanocomposites with [H + P] to TiO$_2$ mass ratios of: [10 + 20]:70 (black line); [15 + 15]:70 (red line); and [20 + 10]:70 (blue line). (P: palygorskite, A: anatase, H: halloysite). (For interpretation of the references to color in this figure legend, the reader is referred to the web version of this article.)

Fig. 2. ATR–FTIR spectra of all the three phase nanocomposites, Hal20:Pal10-TiO$_2$; Hal15:Pal15-TiO$_2$ and Hal10:Pal20-TiO$_2$.

conditions, which neither requires stabilizing agents nor clay calcination. We performed an evaluation of their photocatalytic efficiency in decomposing NO$_x$ gas, an important air pollutant which contributes to the formation of acid rain and to stratospheric ozone destruction and in toluene vapor photo-elimination, as the latter is one of the most prevalent and harmful volatile organic compounds typical of urban atmospheres. The aim of this study is to examine if the mixture of the two clay minerals (double clay nanocomposites) can lead to increased photocatalytic activity compared to the single-clay nanocomposites (clay-based nanocomposites). The latter have been thoroughly studied by many investigators while double clay nanocomposites are prepared and studied here for the first time.

2. Experimental

2.1. Nanocomposites preparation

A halloysite sample from Limnos island Greece and a palygorskite sample from Ventzia continental basin, Western Macedonia, Greece were used. The samples were size fractionated to obtain particles <2 µm by gravity sedimentation. Separation of the clay fraction was carried out by using centrifugation methods. The clay fractions of the samples were used for the preparation of the nanocomposites in order to avoid other mineral impurities.

A stock sol of TiO$_2$ precursor dispersion was prepared by mixing titanium tetraisopropoxide, [Ti(OC$_3$H$_7$)$_4$–TTIP], with hydrochloric acid, 3 distilled water (3D) and absolute ethanol [13]. TTIP concentration was 0.4 M while H$_2$O/TTIP molar ratio was kept 0.82. PH of the sol was 1.27 after HCl addition. The dispersion was diluted with absolute ethanol to give a 0.05 mol/l final concentration of TTIP.

The clay-water dispersion (1% w/w) was stirred for 2 h and an aliquot of TiO$_2$ sol was added to the dispersion in order to obtain a final TiO$_2$ content of 70% w/w. The slurry was stirred for 24 h and the resulting dispersion was centrifuged for 10 min (3800 rpm) followed by three times centrifuge washing with nanopure water. The clay–TiO$_2$ composite was then dispersed in a 1:1 water:ethanol solution, prior to hydrothermal treatment in an autoclave for 5 h (180 °C). The product was centrifuged again for 15 min (at 3800 rpm), and oven-dried for 3 h (at 60 °C). The obtained three-phase [halloysite + palygorskite]–TiO$_2$
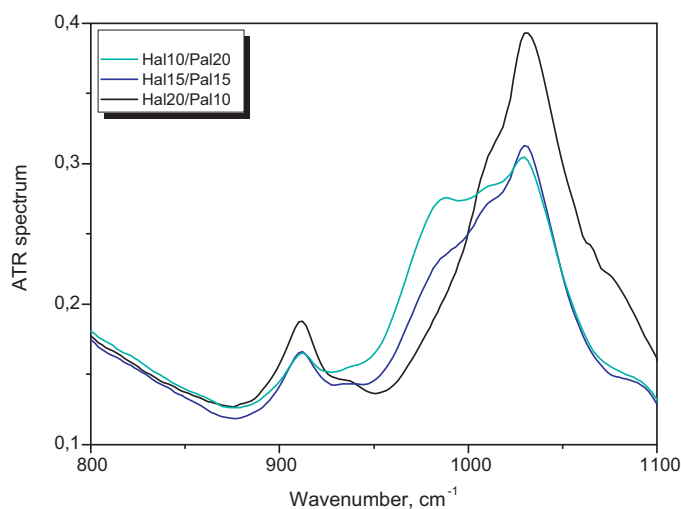
nanocomposites are hereinafter designated as Hal20:Pal10, Hal15:Pal15 and Hal10:Pal20 for halloysite 20% palygorskite 10%, halloysite 15% palygorskite 15% and halloysite 10% palygorskite 20%, respectively. Anatase amount is 70% in every sample.

2.2. Nanocomposites characterization

The phase composition of all samples was determined by X-ray diffraction (using a Bruker D8 advance diffractometer, with Ni-filtered Cu K_α radiation). XRD patterns were obtained from oriented or random powder samples in a 2θ range of 2° to 60° at a scanning rate of 2°/min. Random powder mounts for selected samples were prepared by gently pressing the powder into the cavity holder. Oriented clay powder samples were prepared by the dropper method. The size of the anatase nanoparticles was estimated by using Scherrer's formula, $D = 0.9\lambda/\beta \cos\theta$, where D is the anatase crystallite size in nm, λ is the radiation wavelength (0.154 nm for Cu K_α used), β is the full width at half-maximum and θ is the diffraction peak angle.

Morphology and chemical composition were examined using a scanning electron microscope (SEM JEOL 6300) equipped with an energy dispersive spectrometer (EDS). The chemical composition of the phases by EDS was determined using natural and synthetic standards and 20 kV accelerating voltage with 10 nA beam current. Microanalyses were performed on epoxy resin-impregnated polished, and gold or carbon coated thin sections and sample powders were mounted directly on the sample holder. Morphology and chemical composition of clay minerals were also examined with a SEM LEO SUPRA 35VP. Morphology of a few samples was also determined by transmission electron microscopy (TEM, Model 2010, JEOL, Tokyo, Japan).

Attenuated total reflection infrared (ATR/FTIR) measurements were made with the ATR Miracle accessory of PIKE technologies (diamond crystal) attached to the EQUINOX 55 FT-IR spectrometer (BRUKER). It is interesting to note that ATR–FTIR spectroscopy is suitable for characterization of materials, which are either too thick or too strongly absorbing to be analyzed by TEM and no sample preparation is required.

Nitrogen adsorption–desorption isotherms for each sample degassed at 100 °C for 3 h were obtained at 77 K using Autosorb^{-1} (Quantachrome corporation). Brunauer–Emmet–Teller (BET) surface areas and pore size distribution were determined from the isotherms. Pore size distribution of each sample was obtained using
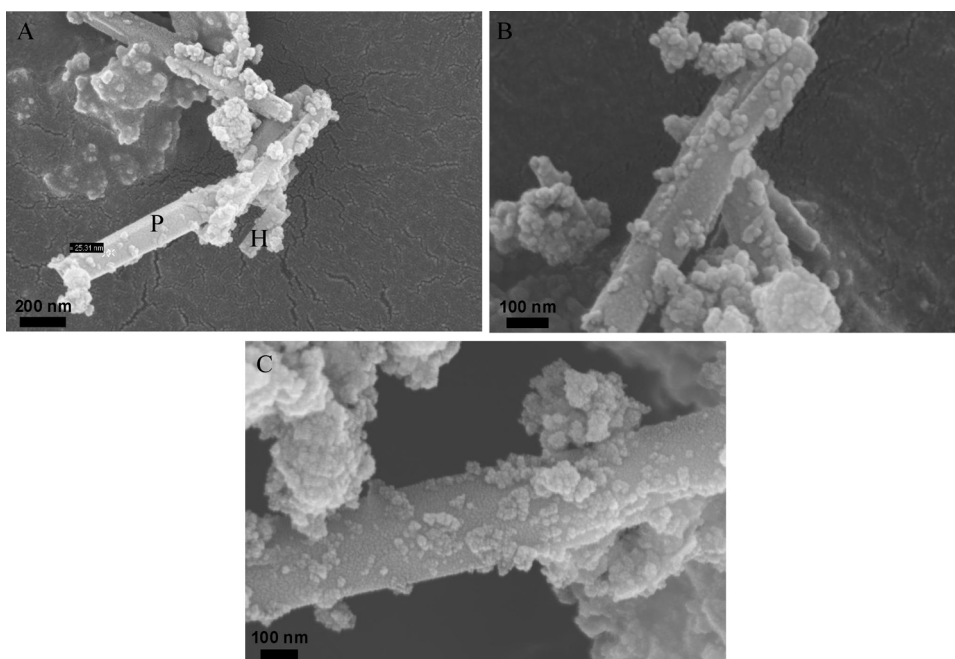
Fig. 3. SEM micrographs showing the three phase nanocomposites: (a) Hal20:Pal10-TiO$_2$ (TiO$_2$ grains are measured to be about 25 nm in a palygorskite crystal); (b) Hal15:Pal15-TiO$_2$; (c) Hal10:Pal20-TiO$_2$. P: palygorskite, H: halloysite.

density functional theory (DFT) method in which a N$_2$ adsorption branch model was selected.

2.3. Photocatalytic activity

The photocatalytic activity for nitrogen monoxide destruction was determined by measuring the concentration of NO gas at the outlet of the reactor (373 cm^3 of internal volume) during the photo-irradiation of a constant flow (200 cm^3/min) of a mixture containing 1 ppm NO—50 vol% air (balance N$_2$). The photocatalyst was placed in a hollow of 20 mm length × 16 mm width × 0.5 mm depth of a glass holder plate and set in the bottom center of the reactor. The photocatalyst under test was first equilibrated with the flowing NO gas before turning on the light. A 450 W high-pressure mercury lamp was used as the light source. The wavelength was controlled by selecting filters, i.e. Pyrex glass for >290 nm, Kenko L41 Super Pro (W) filter >400 nm and Fuji triacetyl cellulose filter >510 nm. The concentration of NO was determined using a NO$_x$ analyzer (Yanaco, ECL-88A). It has been reported that during the photocatalytic destruction, about 20% of NO is directly reduced to N$_2$, and the other 80% is oxidized to NO$_3$ species [14]. For comparison, the photocatalytic reaction was also carried out using the standard commercial titania, Degussa P25.

Activity and selectivity for the gas-phase photo-oxidation of toluene were tested in a continuous flow annular photoreactor [15,16] containing ca. 40 mg of photocatalyst as a thin layer coating on a Pyrex tube. The corresponding amount of catalyst was suspended in 1 ml of ethanol, painted on a Pyrex tube (cut-off at ca. 290 nm) and dried at room temperature. The reacting mixture (100 ml/min) was prepared by injecting toluene (Panreac, spectroscopic grade) into a wet (ca. 75% relative humidity) 20 vol% O$_2$/N$_2$ flow before entering to the photoreactor at room temperature, yielding an organic inlet concentration of ca. 800 ppmv. After flowing the mixture for 3–4 h in the dark (control test), the catalyst was irradiated by four lamps symmetrically positioned outside the photoreactor. The photocatalytic tests were performed under pure UV-light irradiation (Philips TL 6W/08) as well as under a radiation spectrum

simulating sunlight (Philips TL 6W/54-765). At initial reaction times (i.e. <1 h) the photocatalytic oxidation of toluene was greater, which was gradually decreased and stabilized with increasing reaction time. Reaction rates (measured as toluene disappearance) were evaluated under steady state conditions, typically achieved after 4–5 h from the beginning of irradiation. No change in activity was detected for all samples within 24 h after reaching steady state conditions, reflecting the stability of the prepared catalysts under the conditions used. In all cases studied, the C balance was more than 97%. The concentration of reactants and products was analyzed using an on-line gas chromatograph (Agilent GC 6890) equipped with HP-PLOT-Q/HP-Innowax columns (0.5/0.32 mm I.D. × 30 m) and TCD/FID detectors for the quantification of CO$_2$ and organic substances (toluene, photocatalytic products), respectively. The catalytic reactions were conducted in duplicate. Reference reactions containing the untreated halloysite and palygorskite resulted in no toluene degradation.

3. Results and discussion

The XRD patterns of the three nanocomposites confirming the presence of the three constituents of the nanocomposites (palygorskite, halloysite and anatase) and the absence of impurities or any other phase (Fig. 1). The basal reflections of both palygorskite and halloysite (at 10.54 and 7.42 Å, respectively) are relatively small due to their low amount. Anatase reflections are stronger because of its higher amount (70%). The XRD patterns of all three-phase nanocomposites exhibited the characteristic reflections of anatase (γ-TiO$_2$) at 25.3°, 37.9°, 47.6°, 54.8° 2θ. The above observations show that the hydrothermal synthesis conditions of the nanocomposites at 180 °C for 5 h, did not modify the native dehydrated halloysite (halloysite 7 Å) mineral structure. It is well documented [17,18] that heating halloysite (7 Å) at 100–350 °C sharpens the basal reflection and reduces the spacing to 7.2 Å (Fig. 1), but never to as low as 7.14 Å (the characteristic reflection of kaolinite). The temperature of the synthesis is too low to modify the original structure of palygorskite [19] (Fig. 1). The average crystal size of anatase determined
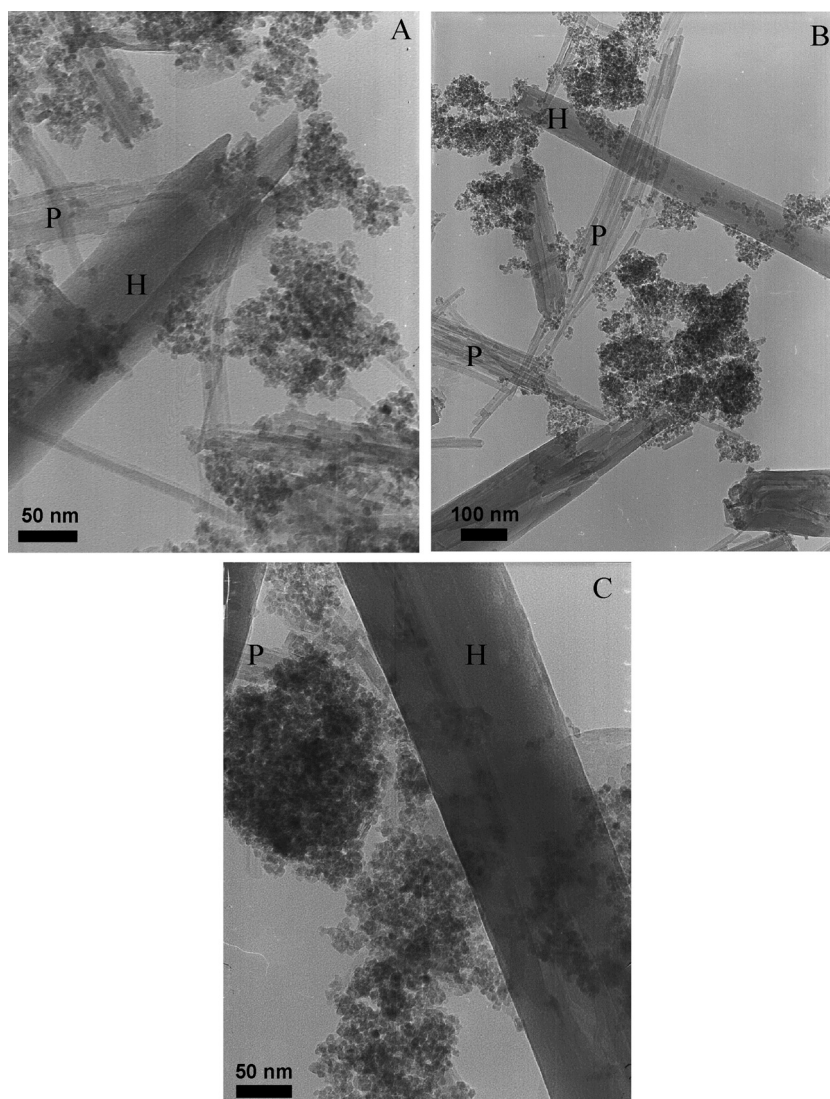
Fig. 4. TEM micrographs showing the three phase nanocomposites: (a) Hal20:Pal10-TiO$_2$; (b) Hal15:Pal15-TiO$_2$; (c) Hal10:Pal20-TiO$_2$. P: palygorskite, H: halloysite.

by XRD (Scherrer's formula) was found to be 4 nm. Because of the coexistence of halloysite as well as palygorskite peaks at the same area (about 25° 2θ) we do not evaluate this value as accurate.

The reflections of the ATR–FTIR spectra indicate that the structures of both palygorskite and halloysite were not significantly changed after the TiO$_2$-treatment procedure (Fig. 2) [18,20]. On the

contrary, the intensity of all bands of palygorskite and halloysite is weakened after the TiO$_2$-treatment, because of the significant decrease in their amount, as it was expected by Beer's law [21]. Differences were only detected for the Si–O stretching bands in both clay minerals. For halloysite Si–O broad stretching band at about 1000 cm^{-1} shifted to 1012 cm^{-1}, probably due to a small distortion of the symmetry of the tetrahedral sheets. Similarly, the band
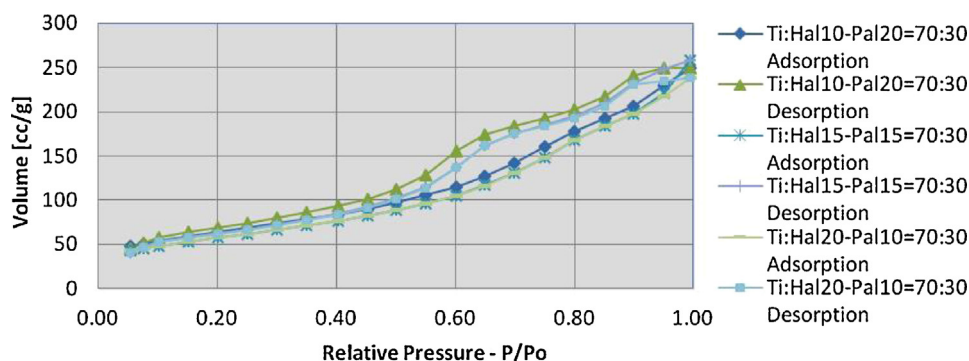

Fig. 5. Nitrogen adsorption (ad)–desorption (de) isotherms the three phase nanocomposites.
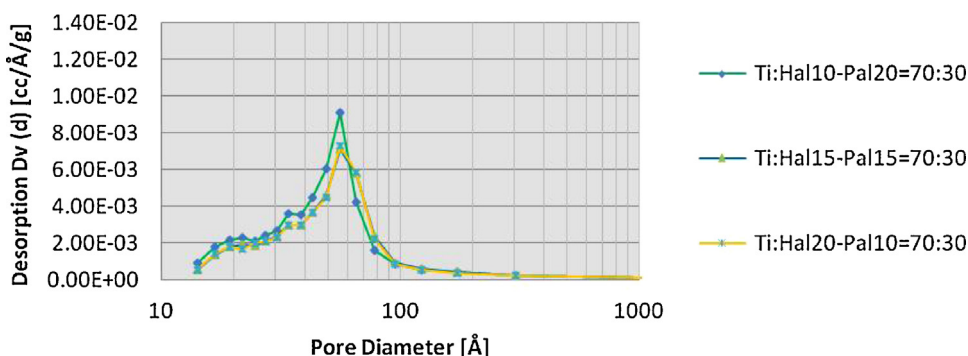
Fig. 6. Pore size distribution curves of the three phase nanocomposites.

Table 1
Pore volume, specific surface area (S_{BET}) and TiO$_2$ content.

Sample	Pore volume (ml/g)	S_{BET} (m^2/g)	TiO$_2$ content (wt%)
Palygorskite	0.81	297	0
Pal30-TiO$_2$70	0.56	242	70
Hal10:Pal20-TiO$_2$70	0.47	228	70
Hal15:Pal15-TiO$_2$70	0.45	207	70
Hal20:Pal10-TiO$_2$70	0.47	206	70
Halloysite	0.44	38	0
Hal30-TiO$_2$70	0.45	167	70

at 974 cm^{-1} attributed to the Si–O bond stretching of palygorskite [22] shifted to about 984 cm^{-1}, indicating a small distortion of the symmetry of the tetrahedral sheets [23]. It should be noted that this band is not clearly observed in the sample containing the lowest amount of palygorskite (10%).

SEM micrographs of the synthesized nanocomposites in comparison with the untreated clay minerals are presented in Fig. 3. SEM micrographs of the untreated palygorskite and halloysite have been presented in previous papers [4,11]. Palygorskite shows matted fibres in planar structures (typical morphology) and halloysite crystals have tubular morphology of about 1 μm in length. The homogeneous distribution of TiO$_2$ grains is anticipated in order to improve the photocatalytic properties of the nanocomposites. SEM observations revealed that most of the uniform TiO$_2$ grains (of about 5–30 nm) were deposited on the treated palygorskite and halloysite particles (Fig. 3a–c). The deposited TiO$_2$ nanoparticles were found to be aggregated on the external surfaces of both the palygorskite and halloysite particles showing no preference to any of these minerals (Fig. 3a–c). It is evident from TEM images (Fig. 4a–c) that TiO$_2$ particles are well dispersed on palygorskite fibres and halloysite tubes, and their grain size varied from 3–10 nm. The TiO$_2$ grain size observed by TEM is in agreement with the values calculated by XRD and significantly smaller than that observed by SEM due to the low resolution of SEM, which showed the presence of some TiO$_2$ aggregates [4]. An interesting observation both by SEM and TEM is that halloysite as well as palygorskite crystals seem that do not agglomerate. This is mainly due to the mixture of two clay minerals with different morphology shape and dimensions. As a result, anatase nanocrystals are better dispersed in these three phase nanocomposites using two nanoclays than in the single-clay based nanocomposites of the same clay minerals, while their presence may act as a spacer between to minerals.

Figs. 5 and 6 show adsorption–desorption isotherms of nitrogen and pore size distributions for all the three-phase nanocomposites. All isotherms are of type IV indicating both meso and micropores (IUPAC classification) [24,25]. The specific surface area (SSA) and the total pore volume of the double clay nanocomposites were found to have intermediate values compared with the (single) clay

based nanocomposites (Table 1, Fig. 6) [4]. The highest values of SSA and total pore volume were observed in the sample containing the highest amount of palygorskite (20%) among the three-phase nanocomposites, due to the fact that untreated palygorskite has much higher SSA and pore volume than halloysite (Table 1). After treating with TiO$_2$, the nanocomposites largely showed mesopores of about 5.7 nm.
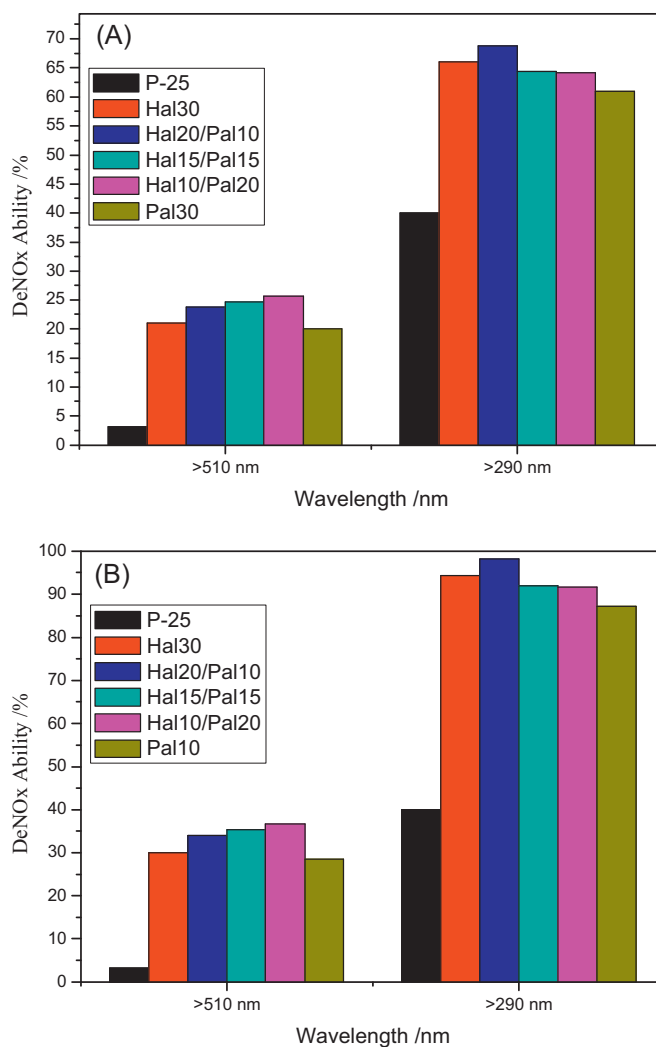

Fig. 7. Photocatalytic activities in decomposing NO$_x$ gas by commercial titania, P-25 and the single clay–TiO$_2$ and three phase nanocomposites based on: (a) the total catalyst's mass and (b) the TiO$_2$ content.
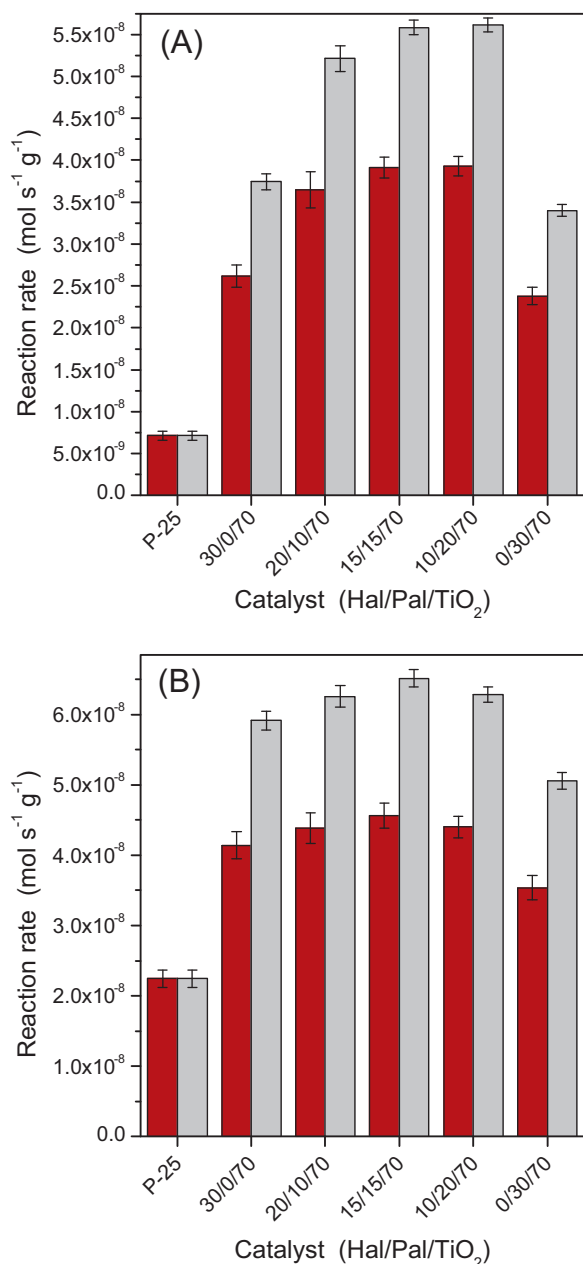
Fig. 9. Diffuse reflectance spectra of commercial titania P-25 and the three phase nanocomposites: (a) P-25; (b) Hal20:Pal10:70TiO$_2$; (c) Hal15:Pal15:70TiO$_2$ and (d) Hal10:Pal20:70TiO$_2$.

Fig. 8. Photocatalytic activities in decomposing toluene by commercial titania P-25 and the single clay–TiO$_2$ and three phase nanocomposites under: (a) artificial solar light and (b) pure UV-light irradiation. Red bars: based on total catalyst's mass; Grey bars: based on TiO$_2$ content. Experimental errors are also set for each sample. (For interpretation of the references to color in this figure legend, the reader is referred to the web version of this article.)

The photocatalytic activities in decomposing NO$_x$ gas are plotted in Fig. 7. Photocatalytic data based on the total catalyst mass, i.e. halloysite + TiO$_2$ presented in Fig. 7a, while data of Fig. 7b are based on the TiO$_2$ content. First to mention is that the three-phase nanocomposites showed significantly higher activity under both visible ($\lambda > 510$ nm) and UV–vis light ($\lambda > 290$ nm) irradiation, up to 8 and 1.72 times, respectively, compared to the commercial titania P-25 (Fig. 7a). These values increase to 11.42 and 2.46 times taking into account the Ti content (Fig. 7b). Most importantly, all the three-phase nanocomposites containing two nanoclays led to higher photoactivity when compared to the single-clay/TiO$_2$ samples under visible light irradiation (Fig. 7).

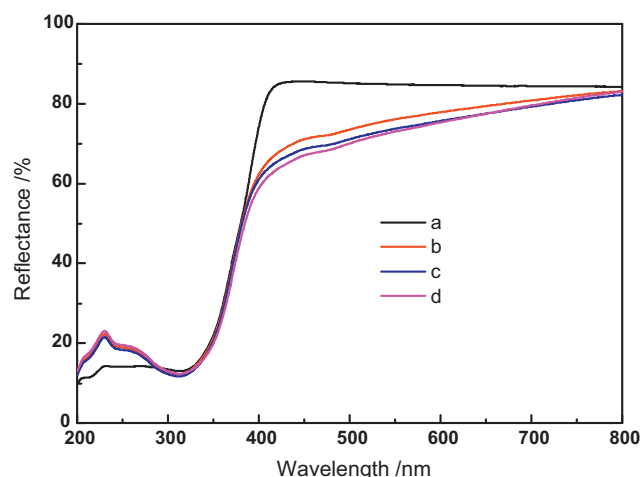The photocatalytic activities in decomposing toluene are plotted in Fig. 8. The three-phase nanocomposites containing two nanoclays showed significantly higher activity compared to the commercial titania P-25, both under artificial solar light (5.5 times) and UV light irradiation (2 times) (Fig. 8, red bars). These values increased to 7.9 and 2.9 times, respectively, on the basis of TiO$_2$ total mass (Fig. 8, grey bars).

Significantly, three-phase nanocomposites containing two nanoclays were more effective than the single-clay based nanocomposites against toluene photo-oxidation. Compared to the palygorskite single-clay nanocomposites, the three-phase nanocomposites containing two nanoclays were 1.7 and 1.3 times more active under artificial solar light and pure UV-light irradiation, respectively. The reaction products of the catalytic tests were also checked. Under the experimental conditions of the present study, the reaction products detected during toluene photo-oxidation were CO$_2$ and benzaldehyde, in agreement with previous results using similar conditions [11,12,15].

In order to investigate the absorption properties of the catalysts, UV–vis reflection spectra were measured, and they are presented in Fig. 9. Commercial titania P-25 showed no absorption in the visible-light region, while the prepared double clay nanocomposites showed a grey colour and absorption in the visible-light region. It can be observed that all samples showed two-step absorption. The first absorption at 410 nm (calculated band gap energy at ~3.0 eV) is attributed to TiO$_2$. The second absorption around 500 nm corresponds to the band gap energy of 2.5 eV. This absorption was probably due to the impurities level caused by carbon doping during the preparation. The absorption of visible light together with the very well dispersed TiO$_2$ on clay mineral surfaces apparently led to the high activity of the prepared catalysts.

Both clay minerals serving as supports play a complex role. On the one hand, they may depress the agglomeration of TiO$_2$ nanoparticles to increase the specific surface area, thereby increasing the catalytic activity; on the other hand, they have a shielding effect, i.e. they scatter or absorb a certain percentage of the incoming UV light, whereby they may decrease catalytic activity [26].

In this study, the increased catalytic activity in UV light suggests that the shielding effect is not significant. It is evident that dispersion of TiO$_2$ on both nanoclay surfaces appears to be highly effective for decomposing NO$_x$ gas and toluene through photocatalytic activity and even higher than using just one of them.

Overall, it is evident from the photocatalytic results of decomposing toluene and NO$_x$ gas that dispersion of TiO$_2$ on both clay mineral surfaces (three-phase nanocomposites) is more effective
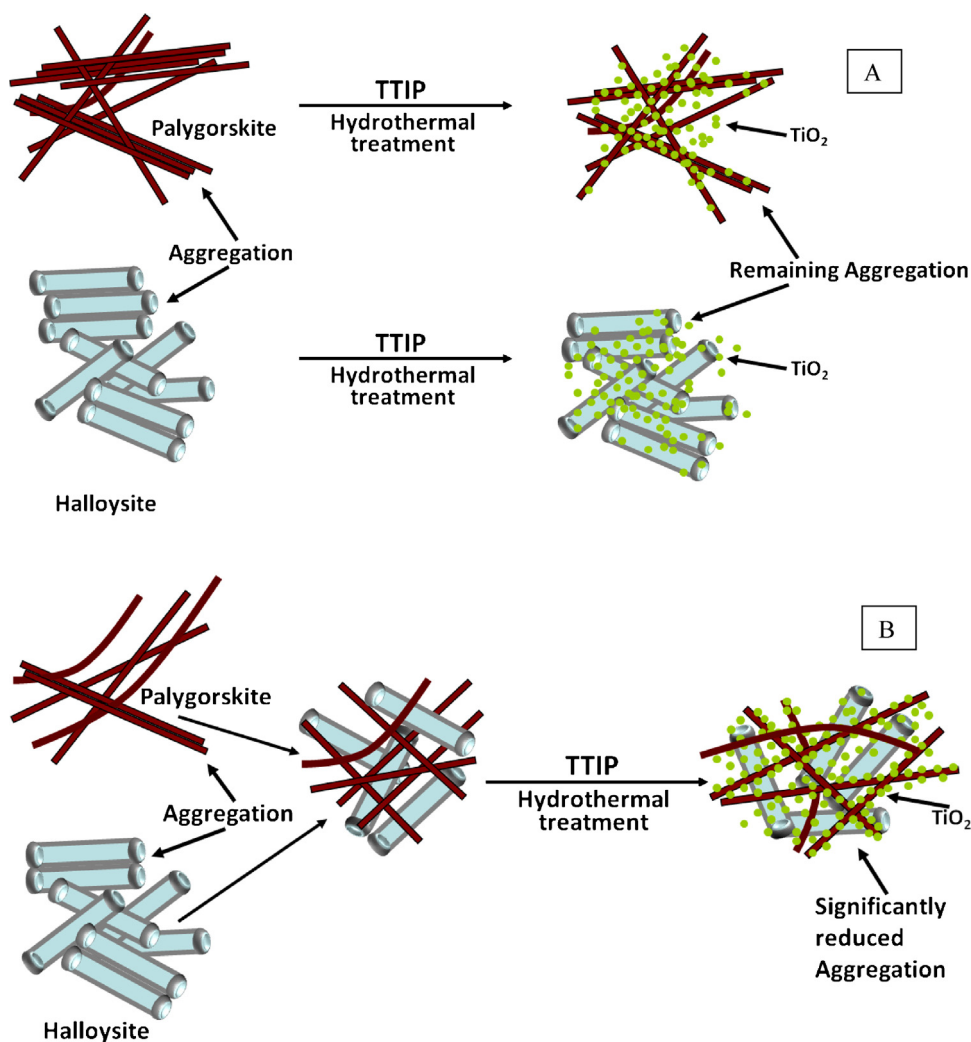
Fig. 10. Schematic representation of the hydrothermal synthesis of: (a) single clay nanocomposites and (b) three phase nanocomposites with two nanoclays, showing the reduced aggregation of clay mineral particles in the novel three phase nanocomposites leading to a better anatase dispersion on clay mineral surfaces.

than using just one of them (single clay–TiO$_2$ nanocomposites). This is attributed to the better dispersion of TiO$_2$ as evidenced by the TEM data (Fig. 4), essentially caused by the less aggregation between the two clay minerals when mixed together compared to the single-clay samples. This resulted in more clay surfaces being available for better anatase dispersion in the three-phase nanocomposites. A schematic representation of the above procedures is presented in Fig. 10.

4. Conclusions

From the present study it is evidenced that the preparation of the novel three-phase nanocomposites with two nanoclays and TiO$_2$ led to better dispersion of TiO$_2$ on the clay surfaces. The three-phase nanocomposites showed significantly higher photocatalytic activity in decomposing both NO$_x$ gas and toluene under visible and UV light irradiation than that of the commercial titania, P-25 and single-clay based nanocomposites with TiO$_2$. This higher activity is attributed to the presence of well-dispersed TiO$_2$, in the form of anatase, on the surfaces of clay minerals. The better dispersion of anatase on the surfaces of clay minerals is due to the different crystal shapes and sizes of the two different nanoclays. The use of two nanoclays led to decreased agglomeration of the clay mineral particles exposing more of their surfaces for the deposition of anatase compared to single-clay based nanocomposites.

References

[1] D. Zhao, J. Zhou, N. Liu, Materials Science and Engineering A: Structural Materials: Properties, Microstructure and Processing 431 (2006) 256–262.
[2] Y. Xuzhuang, D. Yang, Z. Huaiyong, L. Jiangwen, W.N. Martins, R. Frost, L. Daniel, S. Yuenian, Journal of Physical Chemistry C 113 (2009) 8243–8248.
[3] M.J. Martínez-Ortiz, G. Fetter, J.M. Domínguez, Microporous and Mesoporous Materials 58 (2003) 73–80.

[4] D. Papoulis, S. Komarneni, A. Nikolopoulou, P. Tsolis-Katagas, D. Panagiotaras, G.H. Kacandes, P. Zhang, S. Yin, T. Sato, H. Katsuki, Applied Clay Science 50 (2010) 118–124.

[5] C.C. Nascimento, G.R.S. Andrade, E.C. Neves, C.D.F. Santo Barbosa, L.P. Costa, L.S. Barreto, I.F. Gimenez, Journal of Physical Chemistry C 116 (2012) 21992–22000.

[6] D. Kibanova, M. Trejo, H. Destaillats, J. Cervini-Silva, Applied Clay Science 42 (2009) 563–568.

[7] A. Nikolopoulou, D. Papoulis, S. Komarneni, P. Tsolis-Katagas, D. Panagiotaras, G.H. Kacandes, P. Zhang, S. Yin, T. Sato, Applied Clay Science 46 (2009) 363–368.

[8] L. Chmielarz, Z. Piwowarska, P. Kustrowski, B. Gil, A. Adamski, B. Dudek, M. Michalik, Applied Catalysis B: Environmental 91 (2009) 449–459.

[9] L. Chmielarz, Z. Piwowarska, P. Kustrowski, A. Węgrzyn, B. Gil, A. Kowalczyk, B. Dudek, R. Dziembaj, M. Michalik, Applied Clay Science 53 (2011) 164–173.

[10] P. Aranda, R. Kun, M.A. Martín-Luengo, S. Letaïef, I. Dékány, E. Ruiz-Hitzky, Chemistry of Materials 20 (2008) 84–91.

[11] D. Papoulis, S. Komarneni, D. Panagiotaras, A. Nikolopoulou, K.C. Christoforidis, M. Fernandez-Garcia, H. Li, S. Yin, T. Sato, Applied Clay Science (2013), http://dx.doi.org/10.1016/j.clay.2012.03.003, in press.

[12] D. Papoulis, S. Komarneni, D. Panagiotaras, E. Stathatos, D. Toli, K.C. Christoforidis, M. Fernandez-Garcia, H. Li, S. Yin, T. Sato, H. Katsuki, Applied Catalysis B: Environmental 132–133 (2013) 416–422.

[13] M. Langlet, P. Jenouvrier, A. Kim, M. Manso, M. Trejo-Valdez, Journal of Sol–Gel Science and Technology 26 (2003) 759–763.

[14] M. Anpo, in: S. Anpo, A. Syoichi (Eds.), Advanced Developments of Visible Light Response Type Photocatalysts NTS, Tokyo, 2002, p. 9, ISBN: 4-86043-009-03.

[15] K.C. Christoforidis, S.J.A. Figueroa, M. Fernández-García, Applied Catalysis B: Environmental 117–118 (2012) 310–316.

[16] K.C. Christoforidis, A. Iglesias-Juez, S.J.A. Figueroa, M. Di Michiel, M.A. Newton, M. Fernández-García, Catalysis Science and Technology 3 (2013) 626–634.

[17] G.W. Brindley, K. Robinson, Transactions of the Faraday Society 42B (1946) 198–205.

[18] E. Joussein, S. Petit, J. Churchman, B. Theng, D. Righi, B. Delvaux, Clay Minerals 40 (2005) 383–426.

[19] W. Kuang, A.G. Facey, C. Detellier, Clays and Clay Minerals 52 (2004) 635–642.

[20] I. Bobos, J. Duplay, J. Rocha, C. Gomes, Clays and Clay Minerals 49 (2001) 596–607.

[21] S. Petit, Fourier transform infrared spectroscopy, in: F. Bergaya, B.K.G. Theng, G. Lagaly (Eds.), Handbook of Clay Science, 2006, pp. 909–918.

[22] C. Blanco, F. González, C. Pesquera, I. Benito, Spectroscopy Letters 22 (1989) 659–673.

[23] U. Shuali, L. Bram, M. Steinberg, Thermochimica Acta 148 (1989) 445–456.

[24] K.S.W. Sing, D.H. Everett, R.A.W. Haul, L. Moscou, R.A. Pierotti, N. Rouquerol, T. Siemieniewska, Pure and Applied Chemistry 57 (1985) 603–619.

[25] K.S.W. Sing, R.T. Williams, Particle and Particle Systems Characterization (2004) 71–79.

[26] R. Kun, K. Mogyorósi, I. Dékány, Applied Clay Science 32 (2006) 99–110.